Quantum Electronics **49** (1) 43–51 (2019)

https://doi.org/10.1070/QEL16899

Complementary bimodal approach to monitoring of photodynamic therapy with targeted nanoconstructs: numerical simulations

M.Yu. Kirillin, D.A. Kurakina, V.V. Perekatova, A.G. Orlova, E.A. Sergeeva, A.V. Khilov, P.V. Subochev, I.V. Turchin, S. Mallidi, T. Hasan

Abstract. **We propose a new approach to monitoring photodynamic therapy (PDT) of glioblastoma with the use of targeted nanoconstructs containing a photosensitiser (PS) [benzoporphyrin derivative (BPD)] and IRDye800 dye, antibodies for efficient accumulation of the drug in a tumour, and a chemotherapeutic agent for combined effect on tumour cells. Application of IRDye800 is determined by the shift of its absorption and fluorescence spectra to the near-IR range with respect to BPD that ensures a higher imaging depth. Monitoring of PDT is based on the simultaneous fluorescence and optoacoustic (OA) imaging. Fluorescence imaging provides visualisation of fluorescence agents with high molecular sensitivity and monitoring of the effectiveness of PDT by PS photobleaching. OA allows one to examine the vascular pattern of the tumour environment, as well as assess the depth of the tumour. IRDye800 is a better contrast agent in comparison to BPD due to red-shifted spectral characteristics and a higher fluorescence quantum yield. Monte Carlo simulations combined for OA simulations with K-wave modelling allowed the feasibility of the complementary approach to be studied and demonstrated that this combination allows one to localise a tumour with a size of 2 mm at depths from 100 μm to 2 mm.**

Keywords: *photodynamic therapy, optoacoustic imaging, fluorescence imaging, targeted nanoconstructs, Monte Carlo simulations.*

1. Introduction

Glioblastoma is the most aggressive and frequent malignant brain tumour amounting to 16% among all neoplasms of the nervous system. The median survival rate for patients with glioblastoma remains low and is less than 15 months. Surgical treatment of this tumour type has a number of significant limitations associated with the invasion of the tumour cells into surrounding normal tissues [1]. The treatment efficacy can be increased by maximum removal of the tumour and the destruction of viable tumour cells in the peritumoural zone with minimal damage to the functionally important brain areas adjacent to the tumour. One of the approaches to the treatment of tumours of difficult localisations is photodynamic therapy (PDT), based on the accumulation of a photosensitiser in the tumour that promotes the generation of cytotoxic singlet oxygen under irradiation with the light of a certain wavelength [2]. PDT can be applied alone or in combination with other approaches, for example, for the destruction of cancer cells in the tumour bed after tumour surgical removal.

Currently, fluorescence diagnostic techniques are employed to more accurately determine the boundaries of malignant neoplasms and to select the necessary resection volume [3]. These techniques are based on the ability of photosensitisers (PS's) to be selectively accumulated in tumour tissues and to fluoresce when interacting with optical radiation of a specific wavelength. It has been shown that the use of fluorescence imaging in the surgery of brain tumours has made it possible to increase survival without recurrence rate [4, 5]. The effectiveness of fluorescence imaging is determined by the selectivity of accumulation of PS's in the tumour. Traditionally, this selectivity is governed by an increased inflow of PS's into the neoplasm due to its high blood content, a facilitated release of PS's from the highly permeable blood vessels of the tumour, and a weak outflow of PS associated with underdevelopment of the tumour lymphatic vessels [6]. However, this mechanism does not always ensure a high contrast of PS accumulation, especially in brain tumours.

One of the main ways to increase the selectivity of PS accumulation in tumour tissues is the development of targeted drugs. This approach is used to increase the effectiveness of antitumour action and minimise the damage to surrounding normal tissues [7–9]. The combination of antibodies, photosensitisers and antitumour drugs in a single structure opens up the possibility to develop multicomponent agents that implement the principle of theranostics and are used for targeted delivery, fluorescence diagnostics and combined treatment with photodynamic therapy and chemotherapy [10].

In clinical practice, the fluorescence imaging method is used to detect tumour boundaries and monitor PS accumulation and photobleaching. This method demonstrates advantages even in comparison with such techniques as positron emission tomography (PET) and magnetic resonance imaging (MRI) [11]. In experimental oncology, fluorescence imaging was used to test perspective contrasting and photodynamic agents and to develop new PDT protocols [12–16].

New possibilities for tumour treatment planning and monitoring are opened by optoacoustic (OA) imaging, a hybrid imaging technique actively developing in recent years [17, 18]. OA imaging provides three-dimensional images of the tissue structure due to the absorption of optical radiation in endogenous (blood, water, fat, lipids) and exogenous chromophores (fluorescent proteins, quantum dots, chemical

M.Yu. Kirillin, D.A. Kurakina, V.V. Perekatova, A.G. Orlova, E.A. Sergeeva, A.V. Khilov, P.V. Subochev, I.V. Turchin Institute of Applied Physics, Russian Academy of Sciences, ul. Ulyanova 46, 603950 Nizhny Novgorod, Russia; e-mail: mkirillin@yandex.ru;
S. Mallidi, T. Hasan Wellman Center for Photomedicine, Massachusetts General Hospital, Harvard Medical School, Boston, MA 02114, USA

Received 8 August 2018; revision received 18 October 2018
Kvantovaya Elektronika **49** (1) 43–51 (2019)
Translated by M.Yu. Kirillin

dyes), combining the advantages of optical (high contrast) and ultrasonic high spatial resolution) approaches [19–21]. The possibility of choosing a probe wavelength in OA imaging provides selectivity in visualising a particular chromophore. Thus, when several probe wavelengths are selected, OA allows for a complementary visualisation of both the tumour itself in its microcirculatory environment and the PS distribution.

Benzoporphyrin derivatives (BPD), a photosensitiser approved for medical use with excitation peak around 690 nm, showed its efficiency in photodynamic therapy treatment of experimental glioblastomas [17]. However, the possibilities of its fluorescence accumulation monitoring are limited by low fluorescence quantum yield [22]. Employment of multicomponent complexes, including BPD as a photodynamic drug and an additional contrast agent for fluorescence and OA imaging, allows one to overcome these restrictions. The infrared dye IRDye800 widely used for preclinical fluorescence imaging studies [23–25] and tested for optoacoustic imaging [26] can be efficiently employed as a contrast agent.

In present paper the concept of a novel complementary approach to the monitoring of glioblastoma treatment with PDT employing targeted nanoconstructs is proposed. The approach is based on the simultaneous use of OA and fluorescence imaging, while nanostructures contain BPD serving as a fluorescence marker and a PS, IRDye800 serving as a contrast agent for fluorescence and OA imaging, antibodies for effective accumulation in the tumour, and a chemotherapeutic agent for combined effects on tumour cells. The possibilities of a complementary approach are demonstrated using Monte Carlo simulations.

2. Materials and methods

2.1. Simulation of fluorescence and optoacoustic imaging techniques

To evaluate the feasibility of the complementary brain imaging in a laboratory animal by fluorescence and optoacoustic imaging techniques, the previously developed Monte Carlo simulations code [16, 27, 28] was modified. The code is implemented in the MATLAB environment, and all the parameters of launched photons are stored in large-size arrays. Since the MATLAB environment is optimised for working with large arrays, the transformation of coordinates and weights of all photons is performed simultaneously implementing operators over arrays. The simulations are performed in full 3D.

In order to simulate the image obtained with the fluorescence imaging technique, a three-dimensional map of the fluorophore distribution in the medium is predefined before the simulation. In voxels containing a fluorophore, the local optical properties (absorption and scattering coefficients) are calculated as the sums of the partial optical properties of the base medium (biotissue) and the fluorophore. At the first stage of the simulation, the Monte Carlo technique is employed to produce a map of the partial absorption of the probe radiation with a given irradiation configuration by the fluorophore. In the second stage, the resulting partial absorption map serves as a distributed source emitting in the fluorescence band. The distribution of the fluorescence response in the medium is simulated at the second stage also using the Monte Carlo technique. In this case, the launching of emission photons by the fluorophore is considered to be isotropic in direction. The result of the simulation is the three-dimensional distribution of the fluorescence emission fluence with the predetermined volume distribution of the emitting fluorophore in the biotissues. The distribution of fluorescence intensity on the surface of the medium is a fluorescence response recorded by the camera in fluorescence imaging.

In simulations of optoacoustic imaging at the first stage, similarly to the case of fluorescence imaging, an absorption map of probe radiation in the medium is calculated. However, in this case, a full absorption map is calculated, unlike partial absorption in the case of fluorescence, since the optoacoustic signal is generated in all absorbing objects in the medium, not only in the fluorophore. In the second stage, based on the derived absorption map, the acoustic response of the medium is modelled. For modelling, the k-Wave package [29] for MATLAB is used, which is recognised as a gold standard for such calculations. The k-Wave is an open source toolbox designed for the time-domain simulation of propagating acoustic waves in 1D, 2D, or 3D. The forward simulations are based on a k-space pseudo-spectral time domain solution to coupled first-order acoustic equations for homogeneous or heterogeneous media. Numerical model can account for both linear and nonlinear wave propagation, an arbitrary distribution of heterogeneous material parameters, and power law acoustic absorption.

2.2. Simulation parameters

The aim of this work is to study the feasibility of complementary monitoring of gliomas in a laboratory animal brain using nanostructures containing a photosensitiser based on benzoporphyrin derivatives and a fluorescent dye IRDye800. Due to its high absorption, IRDye800 is both a fluorescent marker and a contrast agent for OA imaging. The choice of probe and emission wavelengths is based on the absorption and fluorescence spectra of these components of nanoconstructs (Fig. 1), as well as the wavelengths of commercially available lasers and emission filters. Fluorescence excitation wavelengths are chosen based on the parameters of compact and relatively inexpensive laser diodes with a fibre output and a maximum output power of 0.7 W and wavelengths of 690 and 785 nm (Hicurtec, Russia) for BPD and IRDye800, respectively. Emission wavelengths are chosen based on the parameters of emission filters (Semrock, USA) most efficient for cutting off the exciting radiation of laser diodes and detecting fluorescence: $\lambda_0 = 725$ nm, $\Delta\lambda = 40$ nm and $\lambda_0 = 835$ nm, $\Delta\lambda = 70$ nm for BPD and IRDye800 respectively. To simulate the propagation of the fluorescence response, wavelengths of 725

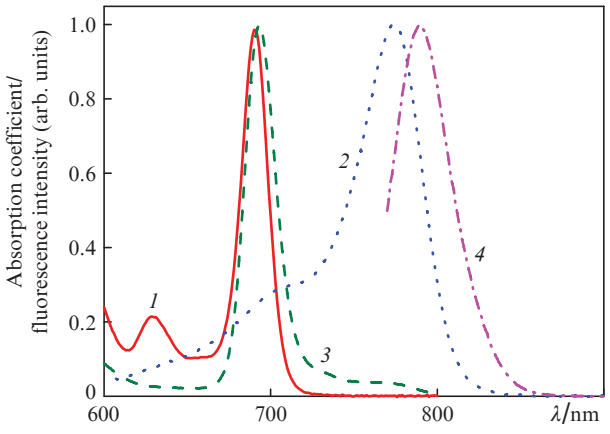

Figure 1. (*1*, *2*) Absorption and (*3*, *4*) fluorescence emission spectra of (*1*, *3*) BPD and (*2*, *4*) IRDye800.

and 835 nm for BPD and IRDye800, respectively, are selected, which corresponds to the conditions for emission registration. The partial absorption coefficients for fluorophores were calculated basing on the absorption spectra of BPD and IRDye800, as well as information about the typical values of their concentration in the tumour upon accumulation.

In simulations it was assumed that the tumour volume amounts about 0.004 mL (spherical tumour with a 1 mm radius) given the total mouse volume of 20 mL. The calculations took into account that, since the agents are delivered to the tumour with nanoconstructs containing antibodies that provide targeted delivery of the drug to the tumour, the tumour accumulates approximately 2% of the drug injected into the animal that is in quantitative agreement with data reported in [30]. Thus, the contrast of drug accumulation in a tumour with respect to normal tissues amounts 100:1. Absorption coefficients μ_a of the studied fluorescence markers in these concentrations are listed in Table 1. It was assumed that BPD is administered into the animal in the amount of 13.6 nmol, and then the drug is accumulated in the tumour with the specified contrast, and the absorption coefficient was calculated based on BPD absorption spectrum [22]. The partial absorption coefficient if IRDye800 was calculated based on the known ratio of concentrations of these components in nanoconstructs. The effect of fluorescence reabsorption is neglected in the simulations, since the absorption at the emission wavelength is significantly smaller than that at the excitation wavelength.

Table 1. Absorption coefficients of fluorescent dyes BPD and IRDye800 at wavelengths of fluorescence excitation and emission.

Fluorescent dye	Wavelength	μ_a/mm^{-1}
BPD	λ_{ex} = 690 nm	0.12
	λ_{em} = 725 nm	0.001
IRDye800	λ_{ex} = 785 nm	0.228
	λ_{em} = 835 nm	0.02

Optical properties of a laboratory mouse brain were chosen as parameters of the base medium. The values were derived from spectrophotometric measurements of brain tissue from a laboratory mouse *ex vivo* [31] and subsequent application of the inverse Monte Carlo technique. The measurements were performed with a Specord 250Plus spectrophotometer (Analytik Jena, Germany) equipped with an integrating sphere. The selected values of the optical properties of the laboratory mouse brain for selected wavelengths are summarised in Table 2.

The model tumour was considered to have a spherical shape with a radius of 1 mm, while the tumour depth z_s (the distance from the tumour point closest to the surface to the surface) ranged from 100 μm to 2 mm. Both for fluorescence and OA imaging it was considered that the probing area is illuminated uniformly, i.e. with a planar wave. In OA imaging simulations, the spherical focused antenna of radius $R = 6.7$ mm with numerical aperture NA = 0.6 is used. The acoustic part of OA imaging simulations was implemented using the MATLAB k-Wave software package [29] on the spatial-temporal grid $(12.4 \times 7.6 \times 12.7 \text{ mm}) \times (10 \text{ μs})$. The simulations were performed for various antenna focus positions z_f relative to the object surface. The geometry of the numerical simulation for two typical positions of the antenna focus is shown in Fig. 2.

Table 2. Optical properties of murine brain *ex vivo* at wavelengths of excitation and detection of BPD (690 and 725 nm, respectively) and IRDy800 (785 and 835 nm, respectively) fluorescence.

Wavelength/nm	μ_a/mm^{-1}	μ_s/mm^{-1}	g	n
690	0.09	8.9	0.78	1.4
725	0.07	8.6	0.78	1.4
785	0.06	8.7	0.80	1.4
835	0.05	8.7	0.81	1.4

Note: μ_s is the scattering coefficient; g is the anisotropy factor; n is the refractive index.

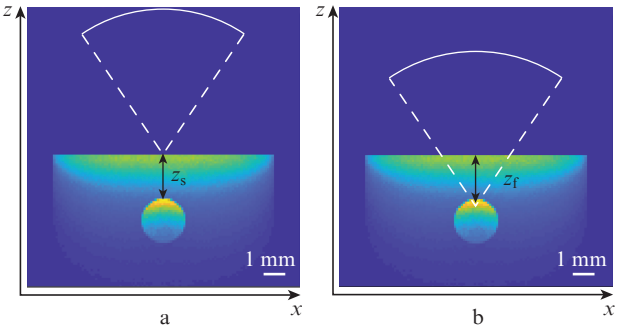

Figure 2. (Colour online) Typical positions of the acoustic antenna focus in OA imaging simulations for a tumour located at the depth $z_s = 2$ mm combined with absorption maps: (a) focus at the surface ($z_f = 0$ mm) and (b) focus at the depth of tumour ($z_f = 2$ mm).

3. Results and discussion

3.1. Fluorescence imaging

The study of feasibility of fluorescence imaging in the visualisation of glioma labelled with nanoconstructs was performed for typical glioma depths z_s varying from 100 μm to 2 mm. As already noted above the fluorescence signal originates from the fluorophores contained in the nanoconstructs. Since the drug contains two fluorophores, BPD and IRDye800, characterised by different absorption peaks, two-wave fluorescence imaging can be performed with excitation at the appropriate wavelengths. To obtain a distribution map of the of the fluorescence source, a fluorophore partial absorption map is calculated in the simulation. Typical BPD partial absorption maps are shown in Fig. 3. It is worth noting that due to significant extinction of probe radiation in biotissue, and especially in the glioma region, the distribution of the absorbed dose in the glioma is significantly nonuniform.

Maps of the spatial distribution of the intensity of fluorescence in biological tissues for different glioma depths are shown in Fig. 4. Obviously, with an increase in the tumour embedding depth, both the intensity of the fluorescence source and the fluorescence intensity on the surface of the sample decrease. The latter is registered by a CCD camera of the simulated fluorescence imaging system. Typical images recorded by a camera with a field of view of 10×10 mm are shown in Fig. 5.

As expected, the fluorescence signal drops significantly with increasing tumour depth. For the quantitative analysis, the central cross sections of the detected BPD fluorescence response were averaged over the entire image and plotted separately depending on the tumour depth (Fig. 6a). Similar results for IRDye800 are shown in Fig. 6b.

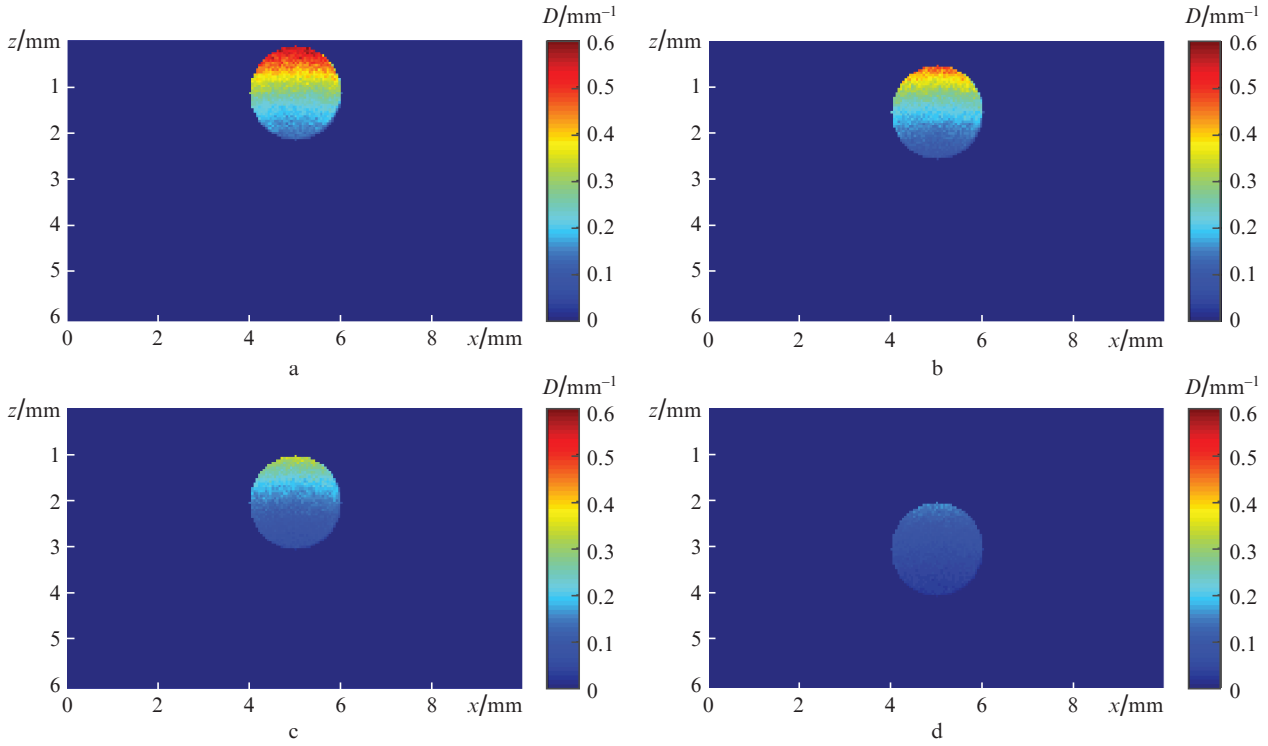

Figure 3. (Colour online) Partial absorption maps for BPD at probe wavelength of 690 nm and different glioma depth of (a) 100 μm, (b) 500 μm, (c) 1 mm and (d) 2 mm. The maps show the ratio D of the number of photons absorbed in a volume unit to the number of launched photons per surface area unit.

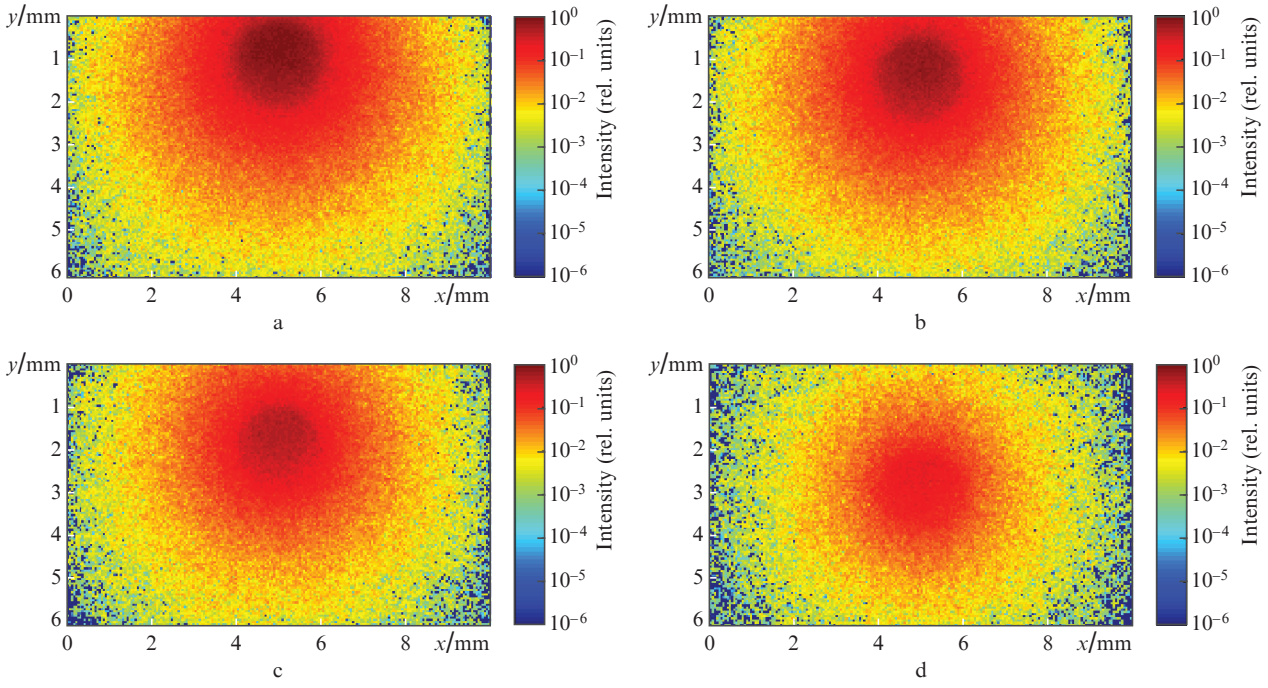

Figure 4. (Colour online) Distribution maps for BPD fluorescence intensity in biotissue for different glioma depth of (a) 100 μm, (b) 500 μm, (c) 1 mm, and (d) 2 mm. The intensity normalised to the intensity of the probe radiation is shown in logarithmic scale for quantum yield equal to 1.

Obviously, the shape of the fluorescence response is determined by both the transverse size of the tumour and tumour embedding depth. One of characteristic parameters that can be employed to derive these tumour characteristics from the fluorescence response image is the response width (HWHM). Dependences of the HWHM characteristic on the tumour embedding depth z_s are shown in Fig. 7 for different tumour radii. One can see that these dependences demonstrate a monotonous increase in HWHM with increasing z_s due to broadening of the fluorescence response originating from multiple scattering in the biotissue layer above the tumour. Another factor of the response broadening is the tumour size,

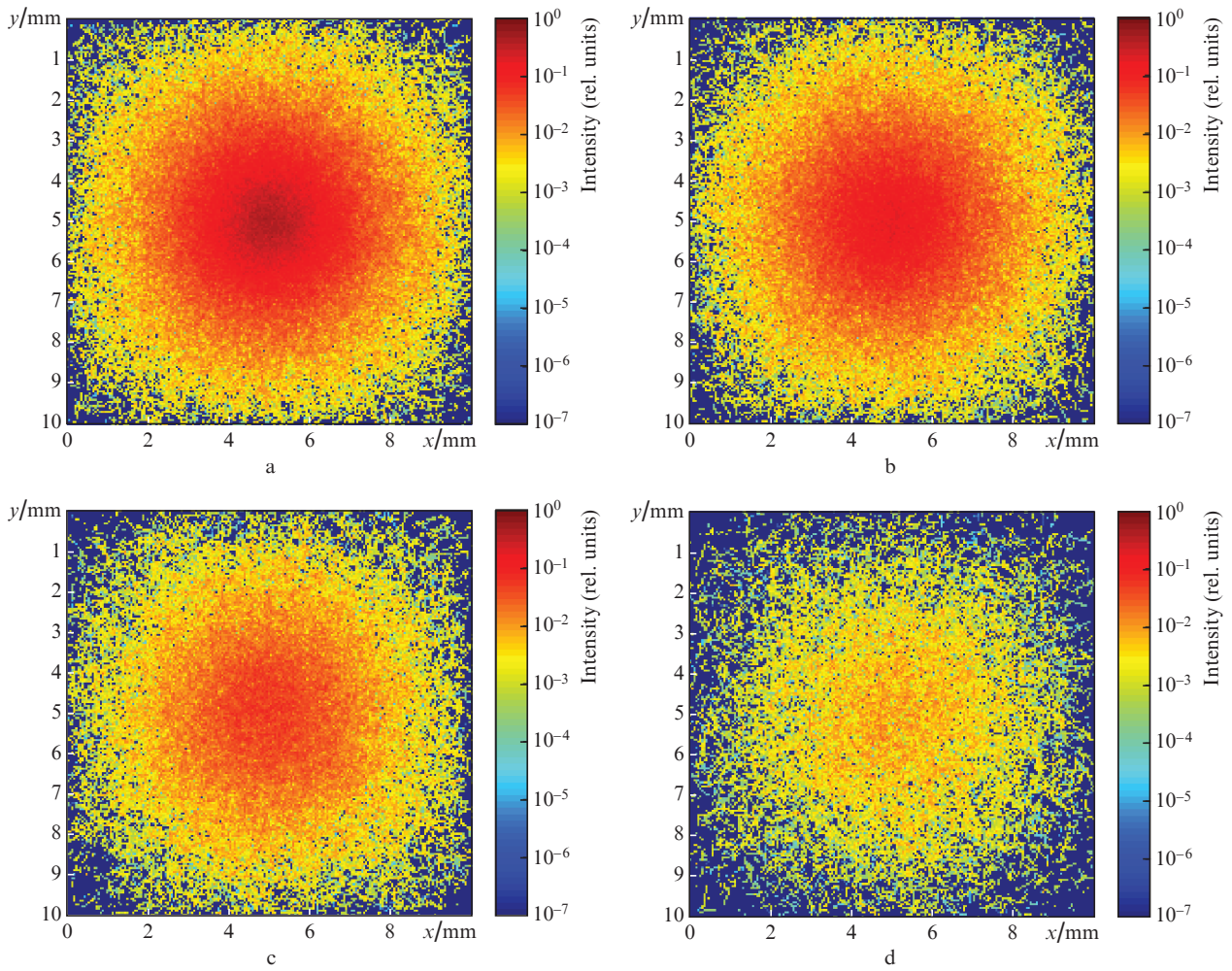

Figure 5. (Colour online) BPD fluorescence responses detected by the fluorescence imaging system CCD camera for different glioma depth of (a) 100 μm, (b) 500 μm, (c) 1 mm, and (d) 2 mm. The intensity normalised to the intensity of the probe radiation is shown in logarithmic scale for quantum yield equal to 1.

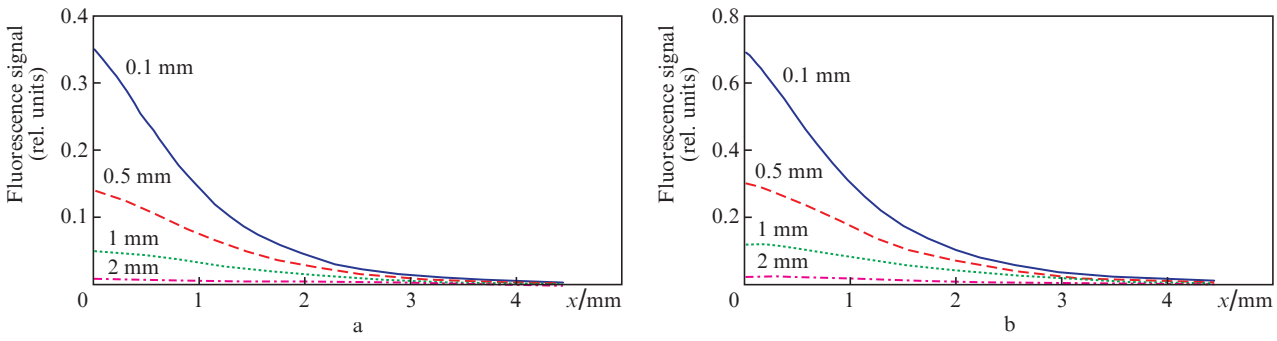

Figure 6. (Colour online) Central cross sections of (a) BPD fluorescence response under excitation at $\lambda = 690$ nm and (b) IRDye800 fluorescence response under excitation at $\lambda = 780$ nm for different glioma depths.

for small z_s values (0.1 and 0.5 mm) this dependence can be clearly seen; however, for large z_s the dependences become distorted due to a low number of detected photons (see Fig. 5d, for example).

An analytical estimation of the signal dependence on depth can be obtained for a point source at a given depth employing diffusion approximation for a semi-infinite medium. In this approximation the radial intensity distribution in fluorescence response on the surface is described by the expression:

$$I(r) = \frac{\exp(-\alpha\sqrt{r^2 + z_s^2})}{\sqrt{r^2 + z_s^2}} - \frac{\exp(-\alpha\sqrt{r^2 + ({}^4/_3 l_{tr} m + z_s)^2})}{\sqrt{r^2 + ({}^4/_3 l_{tr} m + z_s)^2}}, \quad (1)$$

where $\alpha = \sqrt{2\mu_a(\mu_a + \mu_s')}$ is the diffusion extinction coefficient, m is a factor accounting for amplification of the diffuse field due to total internal reflection [32], and $l_{tr} = (\mu_a + \mu_s')^{-1}$ is the transport length. The dependence for HWHM of the fluorescence response for a point source is plotted in Fig.7

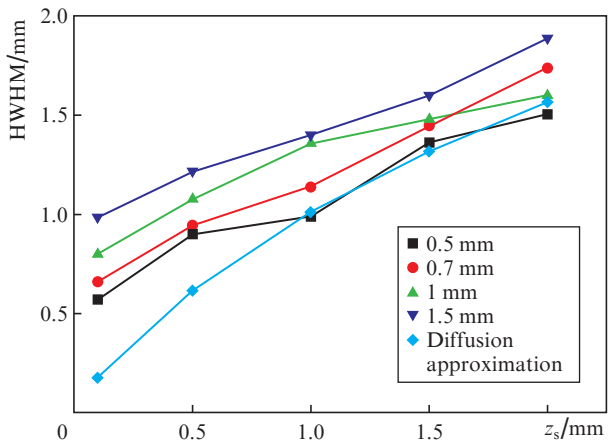

Figure 7. (Colour online) Dependence of the fluorescence response cross-section half-width (HWHM) on the tumour embedding depth for different tumour radii and analytical dependence of the diffusion approximation solution for a point source.

together with the results of Monte Carlo simulations. One can see that the nonzero size of a tumour leads to an increase in HWHM, and this additive factor decreases with increasing tumour depth. Thus, the knowledge of the tumour depth can help in evaluating the tumour size from the fluorescence response image. Complementary employment of OA imaging may provide the information about the tumour embedding depth and, thus, help in evaluating the tumour size.

3.2. Optoacoustic imaging

The probe radiation absorbed in the biotissue serves as a source of OA signal; in this connection, the distributed source map for simulations is calculated as a local pressure map derived from the Monte Carlo absorption map by the formula:

$$p_0(x,y,z) = \frac{\Gamma E_0 A(x,y,z) S}{\Delta V} \text{ [kPa]}, \quad (2)$$

where $\Gamma = 0.2$ is the Grüneisen parameter; $E_0 = 3$ mJ cm^{-2} is the energy density in the probe pulse, $A(x,y,z)$ is the fraction of absorbed energy in the voxel (the absorption map); $S = 0.79$ cm^2 is the area of probing beam illumination on the surface of the medium; and V is the voxel volume. Maps of local pressure distribution obtained by probing biotissue with glioma labelled with IRDye800 are shown in Fig. 8 in the linear scale.

It should be noted that in the case of uniform illumination of the surface and uniform distribution of the agent in glioma, the distribution of absorbed energy in the glioma is substantially nonuniform, and the major part of the energy is absorbed in the glioma region closest to the surface. Thus, the prevailing OA signal is to be expected precisely from the glioma surface, rather than from its entire volume. The simulated raw OA images obtained in the k-Wave toolbox from the pressure distribution maps are shown in Fig. 9. These images demonstrate that absorption in the biotissue superficial layers gives a major contribution to the images obtained; moreover, typical artifacts originating from employment of a spherical acoustic antenna are present in the image. In this connection, the reconstruction of OA images based on the synthetic aperture technique is usually applied [33]. The reconstructed simulated images are shown in Fig. 10; after the reconstruction the signal from the tumour upper boundary can be distinguished (Figs 10b and 10c), and its intensity drops with increasing tumour embedding depth z_s. These simulations demonstrate that while OA imaging does not provide imaging of the entire tumour volume for given parameters (probe wavelength and tumour size), it allows one to evaluate the tumour embedding depth.

For a more detailed quantitative analysis of the effect of the antenna focus position z_f and the tumour embedding depth

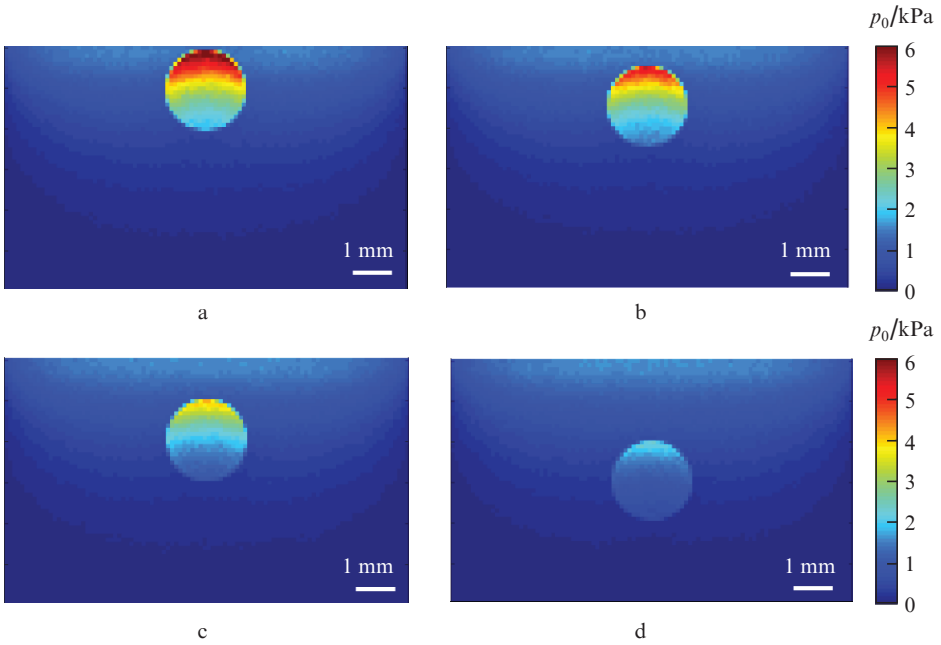

Figure 8. (Colour online) Local pressure distribution maps in biotissue containing glioma labelled by IRDye800 located at different depths of (a) 100 μm, (b) 500 μm, (c) 1 mm, and (d) 2 mm for a probe wavelength of 800 nm.

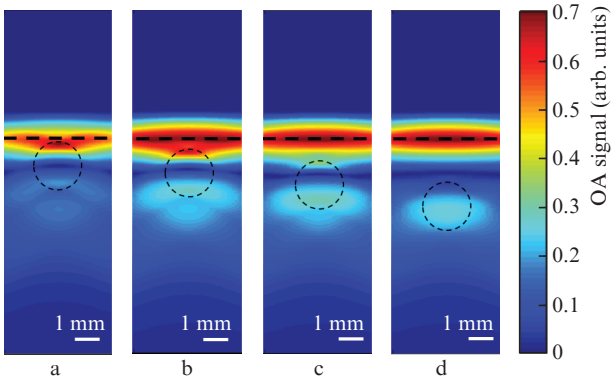

Figure 9. (Colour online) Raw OA images with the focus of the acoustic antenna at a depth 1 mm (dashed line) from the surface for various tumour embedding depths of (a) 100 μm, (b) 500 μm, (c) 1 mm, and (d) 2 mm.

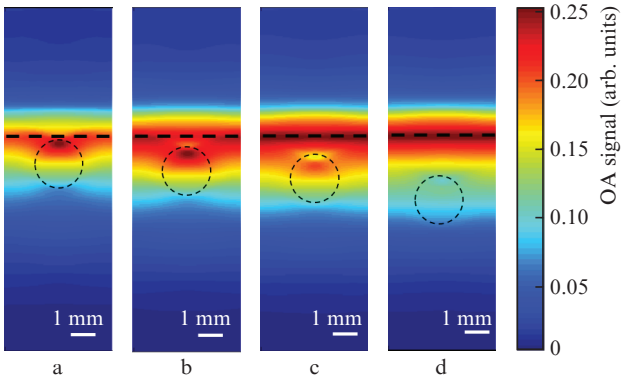

Figure 10. (Colour online) Reconstructed OA images with the acoustic antenna focus at a depth of 1 mm (dashed line) from the surface for various tumour embedding depths of (a) 100 μm, (b) 500 μm, (c) 1 mm, and (d) 2 mm.

z_s on the OA signal, central pressure time series (A-scans) of the reconstructed OA images were plotted (Fig. 11) where zero depth corresponds to the medium surface. For a tumour embedding depth of 100 μm (Fig. 11a), the second, maximum peak is a signal from the tumour upper border (for large focus depths z_f it degenerates into a single peak), while the first peak corresponding to the signal from the tissue surface is weakly pronounced. For large tumour embedding depths, the signal from the medium surface peak (the first peak) remains practically unchanged, and starting from $z_f = 1$ mm, it becomes higher than the second peak corresponding to the tumour boundary. It should be noted that on all presented A-scans for all focus positions, the upper border of the tumour is distinguished.

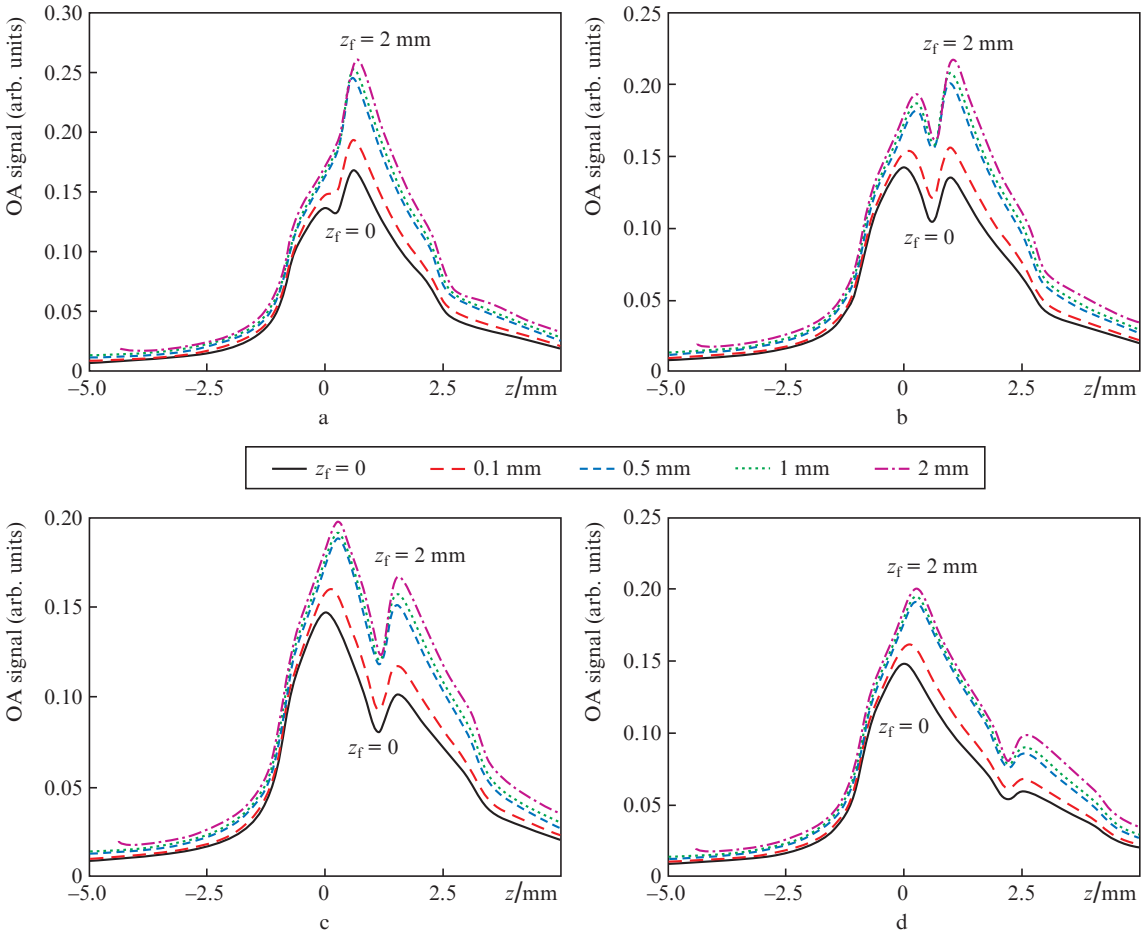

Figure 11. (Colour online) Central A-scans of the reconstructed OA images for various acoustic antenna focus depths and z_s = (a) 100 μm, (b) 500 μm, (c) 1 mm, and (d) 2 mm.

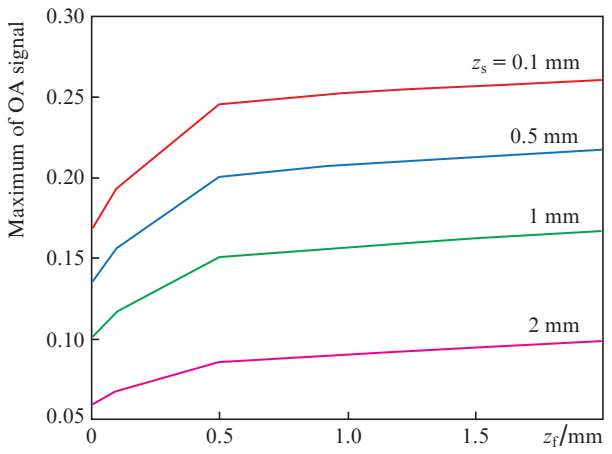

Figure 12. (Colour online) Dependences of the OA signal from the upper tumour boundary on the acoustic antenna focus depths z_f for various tumour embedding depths z_s.

The dependences of the OA signal from the tumour boundary on the acoustic antenna focus depths z_f for various tumour embedding depths z_s are shown in Fig. 12. One can see that the signal from the tumour boundary monotonously rises with increasing z_f.

4. Conclusions

We have developed a numerical model of the complementary approach to imaging of glioma in laboratory mice labelled with nanoconstructs containing BPD serving both as a fluorescent marker and a PS and IRDye800 serving both as a fluorescent marker and an OA contrasting agent. It is shown that both approaches allow one to localise a tumour with a radius of 1 mm at depths from 100 μm to 2 mm. The advantages of dual-wavelength fluorescence imaging allowing simultaneous observation of BPD and IRDye800 dyes are that after localisation of the drug in the tumour fluorescence monitoring of photodynamic therapy procedure could be performed, and its effectiveness could be evaluated from BPD PS photobleaching. Moreover, by measuring the size of the obtained fluorescence response (HWHM), one can estimate the size of the tumour employing complementary information about the tumour localisation depth obtained from OA inspection. Multiple scattering in the superficial biotissue layers leads to broadening of the registered response shape; however, analytical solution obtained in diffusion approximation allows one to account for this effect given the tumour localisation depth.

A feature of OA imaging consists in the substantial extinction of probe radiation in a tumour labelled with nanoconstructs, which leads to a significantly higher contrast of the upper boundary of the tumour, as compared, for example, with its lower boundary. Due to high absorption at the tumour upper boundary, it is visualised in OA images for all considered tumour localisation depths (0.1–2 mm) and the depth of focus of the acoustic antenna (0–2 mm). In addition, with an appropriate choice of the probe radiation wavelength (traditionally, 532 nm), OA imaging provides mapping of the tumour vascular environment. Thus, the methods under consideration provide complementary information about the size and depth of the tumour, as well as its vascular environment, and their simultaneous application will increase the efficacy of photodynamic therapy treatment of gliomas.

Acknowledgements. The study is supported by the Russian Foundation for Basic Research (Project No. 17-54-33043 onko-a). V. Perekatova acknowledges the support of the International Student Grant of the American Acoustic Society.

References

1. Davis M.E. *Clin. J. Oncol. Nurs.*, **20** (5), S2 (2016).
2. Dolmans D.E., Fukumura D., Jain R.K. *Nat. Rev. Cancer*, **3** (5), 380 (2003).
3. Van Meir E.G., Hadjipanayis C.G., Norden A.D., Shu H.K., Wen P.Y., Olson J.J. *CA: Cancer J. Clin.*, **60** (3), 166 (2010).
4. Stummer W., Pichlmeier U., Meinel T., Wiestler O.D., Zanella F., Reulen H.-J., Group A.-G.S. *Lancet Oncol.*, **7** (4), 392 (2006).
5. Stummer W., Tonn J.-C., Mehdorn H.M., Nestler U., Franz K., Goetz C., Bink A., Pichlmeier U. *J. Neurosurg.*, **114** (3), 613 (2011).
6. Henderson B.W., Dougherty T.J. *Photochem. Photobiol.*, **55** (1), 145 (1992).
7. Zhang S., Yang L., Ling X., Shao P., Wang X., Edwards W.B., Bai M. *Acta Biomater.*, **28**, 160 (2015).
8. Jing H., Weidensteiner C., Reichardt W., Gaedicke S., Zhu X., Grosu A.-L., Kobayashi H., Niedermann G. *Theranostics*, **6** (6), 862 (2016).
9. Obaid G., Broekgaarden M., Bulin A.-L., Huang H.-C., Kuriakose J., Liu J., Hasan T. *Nanoscale*, **8** (25), 12471 (2016).
10. Hasan T. *J. Natl. Compr. Cancer Netw.*, **10** (Suppl. 2), S-23 (2012).
11. Roessler K., Becherer A., Donat M., Cejna M., Zachenhofer I. *Neurol Res.*, **34** (3), 314 (2012).
12. Craig S.E., Wright J., Sloan A.E., Brady-Kalnay S.M. *World Neurosurg.*, **90**, 154 (2016).
13. Spring B.Q., Abu-Yousif A.O., Palanisami A., Rizvi I., Zheng X., Mai Z., Anbil S., Sears R.B., Mensah L.B. *Proc. Natl. Acad. Sci.*, **111** (10), E933 (2014).
14. Mitsunaga M., Nakajima T., Sano K., Choyke P.L., Kobayashi H. *Bioconjugate Chem.*, **23** (3), 604 (2012).
15. Shakhova M., Loginova D., Meller A., Sapunov D., Orlinskaya N., Shakhov A., Khilov A., Kirillin M. *J. Biomed. Opt.*, **23** (9), 091412 (2018).
16. Khilov A., Loginova D., Sergeeva E., Shakhova M., Meller A., Turchin I., Kirillin M.Y. *Sovremennye Tekhnologii v Medicine*, **9** (4), 96 (2017).
17. Mallidi S., Watanabe K., Timerman D., Schoenfeld D., Hasan T. *Theranostics*, **5** (3), 289 (2015).
18. Valluru K.S., Willmann J.K. *Ultrasonography*, **35** (4), 267 (2016).
19. Taruttis A., Ntziachristos V. *Nature Photon.*, **9** (4), 219 (2015).
20. Deán-Ben X., Gottschalk S., McLarney B., Shoham S., Razansky D. *Chem. Soc. Rev.*, **46** (8), 2158 (2017).
21. Subochev P., Prudnikov M., Vorobyev V., Postnikova A., Sergeev E., Perekatova V., Orlova A., Kotomina V., Turchin I. *J. Biomed. Opt.*, **23** (9), 091408 (2018).
22. Aveline B., Hasan T., Redmond R.W. *Photochem. Photobiol.*, **59** (3), 328 (1994).
23. Kovar J.L., Volcheck W., Sevick-Muraca E., Simpson M.A., Olive D.M. *Anal. Biochem.*, **384** (2), 254 (2009).
24. Yang L., Sajja H.K., Cao Z., Qian W., Bender L., Marcus A.I., Lipowska M., Wood W.C., Wang Y.A. *Theranostics*, **4** (1), 106 (2014).
25. Li Y., Du Y., Liu X., Zhang Q., Jing L., Liang X., Chi C., Dai Z., Tian J. *Mol. Imaging*, **14** (7), 356 (2015).
26. Luke G.P., Yeager D., Emelianov S.Y. *Ann. Biomed. Eng.*, **40** (2), 422 (2012).
27. Kirillin M., Perekatova V., Turchin I., Subochev P. *Photoacoustics*, **8**, 59 (2017).
28. Kirillin M.Y., Farhat G., Sergeeva E.A., Kolios M.C., Vitkin A. *Opt. Lett.*, **39** (12), 3472 (2014).
29. Treeby B.E., Cox B.T. *J. Biomed. Opt.*, **15** (2), 021314 (2010).

30. Richter A.M., Waterfield E., Jain A.K., Allison B., Sternberg E.D., Dolphin D., Levy J.G. *Br. J. Cancer*, **63**, 87 (1991).
31. Loginova D.A., Sergeeva E.A., Krainov A., Agrba P.D., Kirillin M.Yu. *Quantum Electron*., **46** (6), 528 (2016) [*Kvantovaya Elektron*., **46** (6), 528 (2016)].
32. Krainov A.D., Mokeeva A.M., Sergeeva E.A., Agrba P.D., Kirillin M.Yu. *Opt. Spectrosc*., **115** (2), 193 (2013) [*Opt. Spektrosk*., **115** (2), 47 (2013)].
33. Jaeger M., Schüpbach S., Gertsch A., Kitz M., Frenz M. *Inverse Probl*., **23** (6), S51 (2007).